COMMUNICATIONS MATERIALS

ARTICLE

https://doi.org/10.1038/s43246-020-00060-8 OPEN

Two-dimensional superconductivity and magnetotransport from topological surface states in $AuSn_4$ semimetal

Dong Shen[1,3], Chia Nung Kuo[2,3], Tien Wei Yang[1], I Nan Chen[1], Chin Shan Lue[2] & Li Min Wang[1]✉

Topological materials such as Dirac or Weyl semimetals are new states of matter characterized by symmetry-protected surface states responsible for exotic low-temperature magnetotransport properties. Here, transport measurements on $AuSn_4$ single crystals, a topological nodal-line semimetal candidate, reveal the presence of two-dimensional superconductivity with a transition temperature T_c ~ 2.40 K. The two-dimensional nature of superconductivity is verified by a Berezinsky–Kosterlitz–Thouless transition, Bose-metal phase, and vortex dynamics interpreted in terms of thermally-assisted flux motion in two dimensions. The normal-state magnetoconductivity at low temperatures is found to be well described by the weak-antilocalization transport formula, which has been commonly observed in topological materials, strongly supporting the scenario that normal-state magnetotransport in $AuSn_4$ is dominated by the surface electrons of topological Dirac-cone states. The entire results are summarized in a phase diagram in the temperature–magnetic field plane, which displays different regimes of transport. The combination of two-dimensional superconductivity and surface-driven magnetotransport suggests the topological nature of superconductivity in $AuSn_4$.

[1] Department of Physics/Graduate Institute of Applied Physics, National Taiwan University, Taipei 10617, Taiwan. [2] Department of Physics, National Cheng Kung University, Tainan 70101, Taiwan. [3] These authors contributed equally: Dong Shen, Chia Nung Kuo. ✉email: liminwang@ntu.edu.tw

Superconductivity in reduced dimensions has attracted great attention since it is not only of importance for exploring attractive quantum phenomena at a novel state but also for potential application for developing superconducting electronics[1,2]. Recently, several new two-dimensional (2D) ultrathin superconducting systems have been realized in different materials and hetero-interfaces[3–9]. Typical transition metal oxide interfaces and interface superconductivity between chalcogenides reported so far include $LaAlO_3/SrTiO_3$ (ref. [3]) and PbTe/PbSe families[4], respectively. In addition, 2D superconductivity has been particularly observed in some micrometer-size flakes with a few-layer thickness, such as exfoliated 1T-MoS_2 (ref. [5]), $NbSe_2$ (ref. [6]), and ZrNCl single crystals[7], or chemical-vapor-deposition-synthesized Mo_2C[8] and $1T_d$-$MoTe_2$ thin films[9]. Otherwise, another novel state of quantum matter, the topological material, has become an important topic in condensed matter physics[10], in which the robust topological surface states are topologically protected against time reversal-invariant perturbations. In particular, the topological Dirac or Weyl semimetals are new states of matter that exhibit a linear band dispersion in the bulk along momentum directions, whose low-energy quasiparticles are the condensed-matter analogs of Dirac and Weyl fermions in relativistic high-energy physics, constituting one of the most popular topics in condensed matter physics[11] and extending towards a new kind of topological materials, namely, topological superconductors (TSs)[12]. In TSs, the opening of the superconducting gap is associated with the emergence of zero-energy excitations that are their own antiparticles[13–15], where their zero-energy states are generally called Majorana-bound states. It has been pointed out that inducing s wave superconductivity on the surface state of a topological material results in a p wave superconductor that hosts Majorana fermions in its vortex cores[13,16]. Motivated by the prospect of creating Majorana fermions, which have potential applications in quantum computations[15], several attempts have been made to induce superconductivity on the surfaces of topological materials using bulk superconductors[17,18] or interface superconductivity induced by the superconducting proximity effect[19]. Recently He et al.[20,21] have reported transport measurements on a Bi_2Te_3/FeTe heterostructure with both non-superconducting materials, which reveal superconductivity at the interface and show the two-dimensional nature of the observed superconductivity with the highest transition temperature around 12 K. More recently, Zhang et al.[22] have further demonstrated that without the fabrication of heterostructure for any proximity effect, the iron-based superconductor $FeTe_{0.55}Se_{0.45}$ (superconducting transition temperature $T_c = 14.5$ K) hosts Dirac-cone-type spin-helical surface states at the Fermi level; the surface states exhibit an s wave superconducting gap below T_c, and reveal 2D topological superconductivity, providing a simple and possibly high-temperature platform for realizing Majorana-bound states.

Recently, a novel topological structure of Dirac node arcs and extremely large magnetoresistance of $>10^4$% have been reported in $PtSn_4$ and $PdSn_4$ semimetals[23–26]; these have been recognized as a new breed of topological materials, namely, topological nodal-line (or nodal loop) semimetals (NLSMs). Meanwhile, $AuSn_4$ is isostructural with the Dirac nodal arc semimetals $PtSn_4$ and $PdSn_4$ (refs. [27,28]), revealing superconductivity with T_c of 2.38 K, as reported in the 1960s[29,30]. Surprisingly few studies have so far been made regarding the superconductivity of $AuSn_4$. Inspired by the obtained topological NLSMs $PtSn_4$ and $PdSn_4$, natural superconductivity in $AuSn_4$ can be regarded as a candidate of topological superconductivity on its surface, as we have noted that the surface states of $FeTe_{0.55}Se_{0.45}$ are 2D topologically superconducting. Therefore it will be intriguing to probe the dimensionality of superconductivity in $AuSn_4$.

In this work, we show that the resulting superconductivity possesses the characteristics of $AuSn_4$ with a T_c of ~2.40 K. The superconductivity exhibits 2D nature by showing evidence of a Berezinsky–Kosterlitz–Thouless (BKT) transition, Bose-metal phase, and the vortex dynamics interpreted in terms of thermally assisted flux motion in two dimensions. Moreover, it is found that in the normal state the low-temperature magnetoconductivity of $AuSn_4$ can be well described by the weak-antilocalization (WAL) transport formula. The results strongly support the concept that the surface electrons in Dirac-cone states dominate the normal-state magnetotransport in $AuSn_4$ single crystals, leading to the observed 2D superconductivity. In contrast to the recently discovered 2D superconductors, which were fabricated in the shape of micrometer-size flakes with a few-layer thickness, the millimeter-size bulk $AuSn_4$ single crystals peculiarly exhibit 2D superconductivity, and display large normal-state magnetoresistance accompanied by high carrier mobility, revealing the advantages of $AuSn_4$ as the key to understanding topological 2D superconductivity.

Results

Structure and bulk superconductivity in $AuSn_4$ single crystals. Figure 1a is a typical picture of the cleaved single crystals, showing millimeter-sized crystals with metallic luster. The crystal structure in real space is schematically shown in Fig. 1b. The

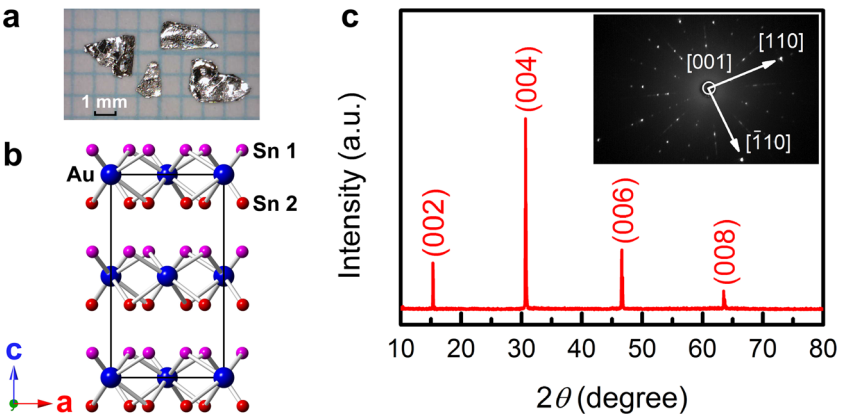

Fig. 1 Crystal structure of $AuSn_4$. **a** A typical picture of the cleaved single crystals. **b** Schematic $AuSn_4$ crystal structure in real space. **c** X-ray θ–2θ diffraction spectrum for a single crystalline $AuSn_4$ specimen. Inset is a photograph of the Laue pattern from the [001] direction for $AuSn_4$, and shows the directions of the crystal axes [110] and [$\bar{1}$10] as indicated.

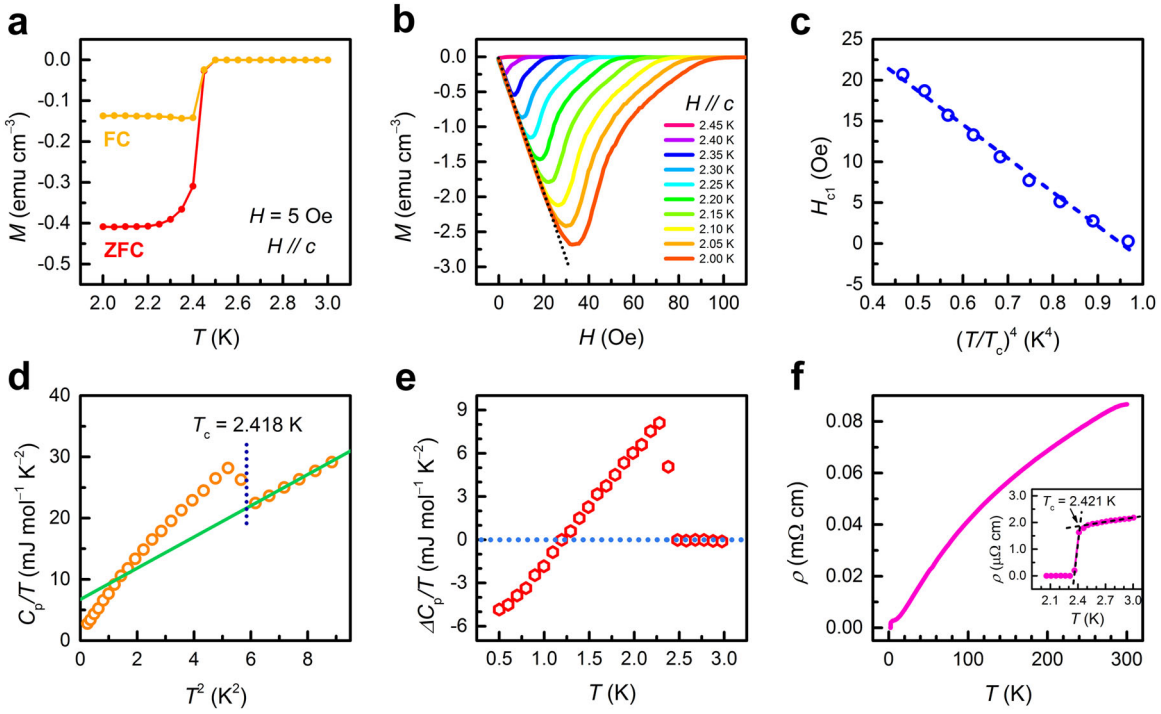

Fig. 2 Magnetic and transport properties of $AuSn_4$. **a** ZFC and FC magnetizations in $H = 5$ Oe parallel to the crystal *c*-axis for an $AuSn_4$ single crystal. **b** Magnetization $M(H)$ curves of $AuSn_4$ at various temperatures in out-of-plane fields. **c** Obtained H_{c1} as a function of reduced temperature $(T/T_c)^4$ for $AuSn_4$ with a solid line showing fit to the data. **d** Low-temperature heat capacity C_p/T vs. T^2 with the red line showing the linear fit in the temperature range of 2.5–3.0 K and the equal-area approximation for the T_c determination. **e** The excess specific heat $\Delta C_p/T$ of superconductivity by subtracting a smooth normal-state background as represented by the red dashed line. **f** Whole temperature range of resistivity for $AuSn_4$. The inset shows $\rho(T)$ in zero field at temperatures near T_c.

crystallographic *c*-axis is anticipated to be perpendicular to the mirrored surface shown in Fig. 1a. Figure 1c shows the X-ray θ–2θ diffraction spectrum for a single crystalline specimen, in which only the $(00n)$ ($n = 2$, 4, 6, and 8) diffraction peaks were observed, indicating that the [001] direction is perpendicular to the plane of the crystals. The lattice constant of the *c*-axis can be determined precisely to be 11.708 Å and is very close to that of 11.707 Å as reported[27]. The inset of Fig. 1c shows the Laue diffraction pattern of single crystalline $AuSn_4$, indicating good crystallization of crystal as judged by the sharp spots in the Laue pattern. All peaks in the diffraction pattern can be well indexed with the orthorhombic *Aea2* space group, with the structure similar to $PtSn_4$.

Figure 2a shows the zero-field-cooling (ZFC) and field-cooling (FC) magnetizations in $H = 5$ Oe parallel to the crystal *c*-axis for an $AuSn_4$ single crystal, demonstrating the observation of superconducting transition temperature $T_c \approx 2.40$ K, which is consistent with a previous report of 2.38 K[29]. The superconducting shielding fraction is estimated to be over 99%, based on the magnetization at 2 K. The smaller FC signal, compared with the ZFC signal, is caused by vortex pinning. Figure 2b shows the measured magnetization $M(H)$ curves of $AuSn_4$ at various temperatures in magnetic fields parallel to the crystal *c*-axis (out-of-plane *H*). The lower critical field H_{c1} is determined by the ≤1% deviation of the $M(H)$ curve from the linear fitting in the even lower-field regime. According to the traditional nodeless Bardeen–Cooper–Schrieffer (BCS) and the two-fluid model theories, the temperature dependence of H_{c1} is proportional to λ^{-2} and can be expressed by $H_{c1}(T) = H_{c1}(0)\ [1 - (T/T_c)^4]$, where λ is the magnetic penetration depth. Figure 2c shows the obtained H_{c1} as a function of reduced temperature $(T/T_c)^4$ for $AuSn_4$, and also shows a good approximation with adopted $H_{c1}(0) = 39.4$ Oe. The temperature dependence of H_{c1} indicates that the bulk superconductivity of $AuSn_4$ resembles that of the s wave BCS superconductor as observed for an NbN film[31]. Bulk superconductivity is also confirmed by a large anomaly at 2.418 K in heat capacity. Figure 2d illustrates the low-temperature heat capacity C_p/T versus T^2 and the equal-area approximation for the T_c determination. The experimental data can fit in the temperature range of 2.5–3.0 K by using the formula $C_p = \gamma T + \beta T^3$, where the electronic specific-heat coefficient (Sommerfeld coefficient) $\gamma = 6.73$ mJ mol^{-1} K^{-2} and phonon specific-heat coefficient $\beta = 2.55$ mJ mol^{-1} K^{-4} were obtained. Figure 2e illustrates the excess specific heat $\Delta C_p/T$ of superconductivity by subtracting a smooth normal-state background, estimated by fitting the specific heat through the data above the superconducting transition region. Using γ and the specific-heat-jump value $\Delta C_p/T_c$ at T_c, $\Delta C_p/\gamma T_c$ could be calculated and was found to be 1.26, which is slightly smaller than the BCS value of 1.43. Figure 2f shows the whole temperature range of resistivity. The normal-state resistivity for $AuSn_4$ reveals a metallic-like character ($d\rho/dT > 0$), with the residual resistivity ratio ≈48. The inset of Fig. 2f shows the temperature dependence of resistivity $\rho(T)$ in zero field at temperatures near T_c. The estimated T_c, as determined by an intersection of two linear fitting lines extrapolated from the normal-state resistivity and resistive transition, respectively, is 2.421 K, which agrees with magnetization and specific heat measurements. It is worth mentioning that samples from different batches of $AuSn_4$ crystals show almost the same superconductivity, as well as the normal-state transport properties (for details, see Supplementary Note 1). The bulk superconductivity of $AuSn_4$, characterized by the magnetization and special heat measurements, reveals a conventional nodeless BCS superconductor. However, the superconductivity explored by

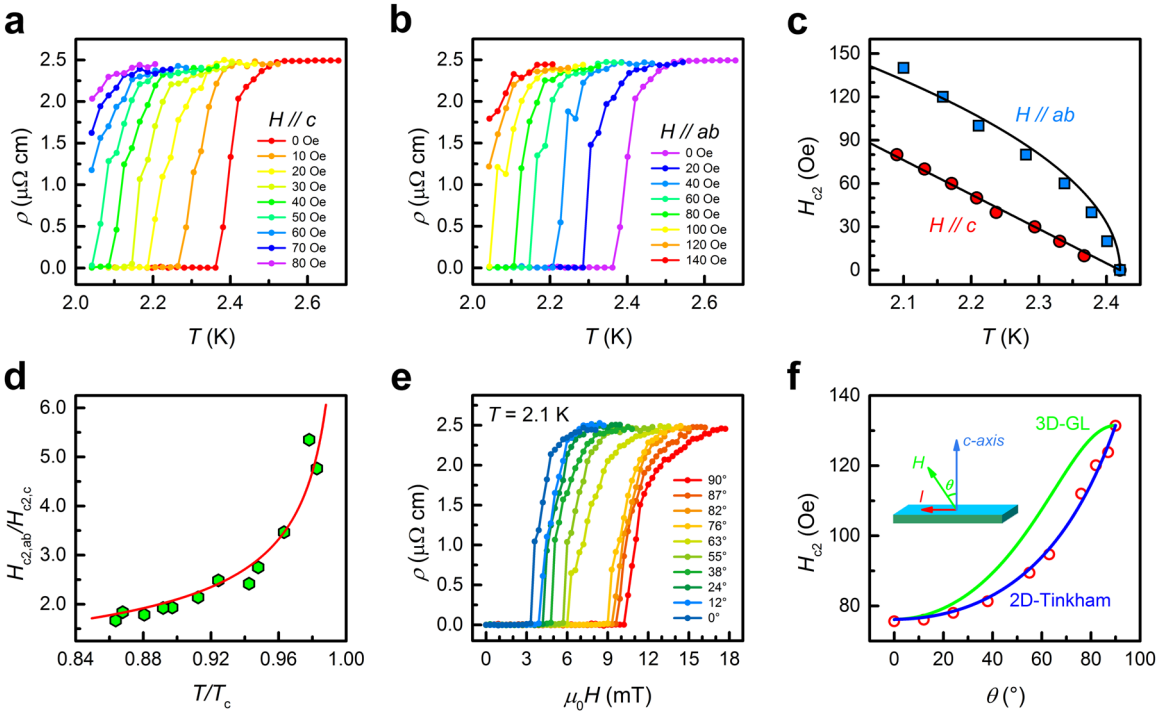

Fig. 3 Mixed-state magnetotransport properties of single crystal $AuSn_4$. Temperature dependence of resistivity in magnetic fields parallel to: **a** the crystal *c*-axis and **b** *ab* plane. **c** Upper critical fields $H_{c2,c}(T)$ and $H_{c2,ab}(T)$ for an $AuSn_4$ crystal. **d** The $H_{c2,ab}/H_{c2,c}$ ratio vs. reduced temperature T/T_c. Solid lines represent the fits to the data. **e** Magnetic field dependence of the resistivity under different θ at 2.1 K. **f** The angular dependence of the upper critical field $H_{c2}(\theta)$, as extracted from **e**. The blue solid line and the green solid line represent the fitting with the 2D Tinkham formula and the 3D anisotropic mass model, respectively. The inset is a schematic drawing of a tilt experimental setup, where θ is the tilted angle between the normal of the sample plane and the direction of the applied magnetic field. The direction of applied current *I* is also indicated.

electrical transport measurement is open to question due to the contribution of the surface conductivity.

Mixed-state magnetotransport properties and 2D superconductivity. Figure 3a, b shows the resistivity as a function of temperature in magnetic fields parallel to the crystal *c*-axis and *ab* plane, respectively. Figure 3c shows the upper critical fields $H_{c2,c}(T)$ and $H_{c2,ab}(T)$ for an $AuSn_4$ crystal in fields parallel to the crystal *c*-axis and *ab* plane, respectively, where the corresponding upper critical field H_{c2} values are derived from the resistive transition in the curves of Fig. 3a, b, like the T_c determination in the inset of Fig. 2f. As seen, $H_{c2,c}(T)$ shows the expected linear *T* dependence, which follows the standard linearized Ginzburg–Landau (GL) theory,

$$H_{c2,c}(T) = \frac{\Phi_0}{2\pi\xi_{GL}(0)^2}\left(1-\frac{T}{T_c}\right) \propto \left(1-\frac{T}{T_c}\right), \qquad (1)$$

where Φ_0 is the flux quantum and $\xi_{GL}(0)$ is the GL coherence length at $T = 0$ K. However, it is noted that upper critical field for $H_{c2,ab}(T)$ follows the GL form of temperature-dependent behavior for 2D superconductors[32]:

$$H_{c2,ab}(T) = \frac{\sqrt{3}\Phi_0}{\pi\xi_{GL}(0)d_{sc}}\left(1-\frac{T}{T_c}\right)^{1/2} \propto \left(1-\frac{T}{T_c}\right)^{1/2}, \qquad (2)$$

where d_{sc} is a corresponding superconducting thickness; the resulting fitting curve is shown in Fig. 3c as well. Using the temperature-dependent H_{c2} relationships of Eqs. (1) and (2), the mean value of $\xi_{GL}(0)$ could be calculated as 75.58 nm, and the mean value of superconducting thickness d_{sc} was then estimated to be 417.2 nm, which is greatly less than the sample thickness *d* of ~100 μm, but larger than $\xi_{GL}(0)$. Regarding the $d > \xi_{GL}(0)$ case, as reported on the GaN/NbN epitaxial semiconductor/superconductor heterostructures[33], it has been proposed that samples may behave like a thin film. In view of the 2D-$H_{c2,ab}(T)$ behavior, let us then consider that the 2D electrical transport may originate from the surface conducting channel within a thickness of d_{sc}. When the temperature approaches the critical temperature, the coherence ξ_{GL} would increase to be larger than d_{sc}, thus, the sample would reach the 2D limit. Taking into account that $\xi_{GL}(T) = \xi_{GL}(0)\cdot(1 - T/T_c)^{-1/2}$, we can estimate the crossover temperature as $d_{sc} = \xi_{GL}$ and have the crossover temperature of $T/T_c = 0.967$, i.e., at $T = 2.32$ K, which is in accordance with the apparent 2D behavior of $H_{c2}(T)$ at $T > 2.30$ K, as shown in Fig. 3c. This result gives a good account of the surface conductivity that can be explored by electrical transport measurements. The derived $H_{c2}(T)$ values were used to plot the $H_{c2,ab}/H_{c2,c}$ ratio versus reduced temperature T/T_c, as seen in Fig. 3d; it does show a diverging characteristic on approaching T_c, characteristic for a 2D nature, as recently observed[5,8,20]. The 2D superconducting behavior is further confirmed by experiments with a tilted magnetic field. Figure 3e shows the magnetic field dependence of the resistivity under different θ at 2.1 K, where θ is the tilted angle between the normal sample plane and the direction of the applied magnetic field (see the inset of Fig. 3f). Clearly, the superconducting transition shifts to a higher field with the external magnetic field rotating from perpendicular $\theta = 0°$ (H // c) to parallel $\theta = 90°$ (H // ab). The upper critical field H_{c2} was extracted from Fig. 3e, and plotted in Fig. 3f, as a function of the tilted angle θ; as seen, a cusp-like peak is clearly observed at $\theta \approx 90°$. The angular dependence of $H_{c2}(\theta)$ was fitted using the 2D Tinkham formula[34] $\left|\frac{H_{c2}(\theta)\cos\theta}{H_{c2,c}}\right| + \left(\frac{H_{c2}(\theta)\sin\theta}{H_{c2,ab}}\right)^2 = 1$ and the three-dimensional anisotropic GL model[35] $\left(\frac{H_{c2}(\theta)\cos\theta}{H_{c2,c}}\right)^2 + \left(\frac{H_{c2}(\theta)\sin\theta}{H_{c2,ab}}\right)^2 = 1$, with the values of $H_{c2,c}$ and $H_{c2,ab}$, as previously obtained. As shown in Fig. 3f, the cusp-shaped dependence can only be well explained with the 2D Tinkham model, further demonstrating that the single-crystal $AuSn_4$ exhibits the 2D nature of superconductivity.

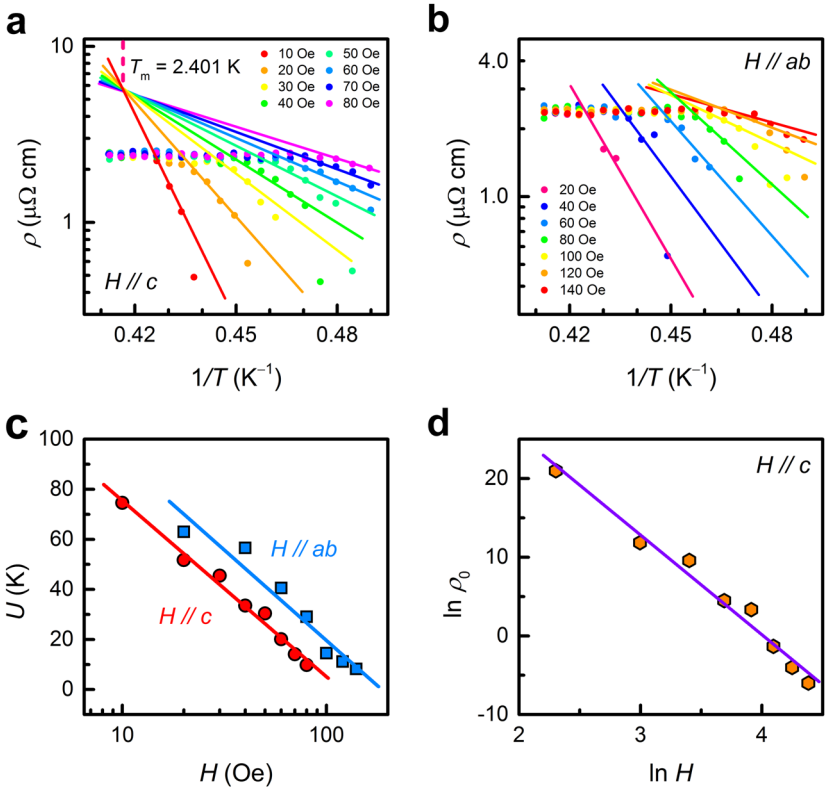

Fig. 4 Arrhenius plot of resistivity for $AuSn_4$. Arrhenius plot of resistivity for $AuSn_4$ in magnetic fields: **a** parallel to the crystal *c*-axis and **b** *ab* plane. Solid lines are corresponding fitting results from the Arrhenius relation. **c** Field-dependent activation energies extracted from the Arrhenius plot of resistivity on a semi-logarithmic scale. Solid lines are fitting results from the function $U(H) = U_0\ \ln(H_0/H)$. **d** A $\ln\rho_0$–$\ln H$ plot extracted from the Arrhenius plot of resistivity with H // *c*-axis. The solid line represents the relation of $\rho_0 \propto H^{-p}$ with $p \approx 12.7$.

In Fig. 3a, b, the resistivity under magnetic field shows a broadening behavior due to thermally activated flux motion, which has been proposed by Anderson and Kim[36], and can be described by: $\rho(T, H) = \rho_0 \exp(-U/k_BT)$. Here U is the activation energy, which is normally both field- and temperature-dependent. In the Anderson–Kim model, the U value is an indication of the magnitude of effective pinning energy. Figure 4a, b shows the Arrhenius plot of resistivity as a function of $1/T$ for $AuSn_4$ in magnetic fields of different magnitudes, parallel to the crystal *c*-axis and *ab* plane, respectively. The resistive transition just below T_c reveals linear behavior in the Arrhenius plot and follows the equation of thermally activated flux motion as highlighted by straight solid lines. In Fig. 4a for resistive transitions in fields parallel to the crystal *c*-axis, all fitting lines in different fields cross to one point, whose corresponding temperature T_m of 2.401 K is close to the T_c of $AuSn_4$, being in agreement with that reported on the Bi_2Te_3/FeTe heterostructures[21]. One may notice the difference that the Arrhenius plots of resistive transitions for H // *ab* plane in Fig. 4b do not show this result, implying that the simple Arrhenius relation can only be satisfied in a narrower region. It is known that the effects of prefactor ρ_0 and nonlinear relation of $U(T, H)$ may lead to $\rho(T, H)$ deviating from Arrhenius relation for H // *ab* plane as seen in Fe(Te,S) single crystals[37]. Figure 4c shows the field-dependent U extracted from Anderson and Kim's theory, in which $U(H)$ is plotted as a function of the magnetic field on a semi-logarithmic scale. As seen, $U(H)$ decreases monotonically with increased magnetic field due to an increase of vortex density and interaction between the vortices. It is found that the field dependence of activation energy U can be written as $U(H) = U_0\ \ln(H_0/H)$ with $U_0 =$ 30.54 (31.35) K and $H_0 = 118.3$ (186.9) Oe for H // *c*-axis (H // *ab* plane). It has been pointed out that in clean 2D superconductors, U is expected to follow a logarithmic dependence on the magnetic field, based on collective flux creep model[38]. As shown in Fig. 4c, a linear relationship of $U(H) \propto -\ln H$ is observed, in accordance with the model of thermally assisted collective flux motion in two dimensions, as recently observed in other 2D crystalline superconductors[5–8]. Figure 4d shows a $\ln\rho_0$–$\ln H$ plot extracted from the Arrhenius plot of resistivity with H // *c*-axis, and illustrates the obtained result that ρ_0 is proportional to H^{-p} with $p \approx 12.7$, consistent with the calculation of $p = U_0/k_BT_m$ derived from the Anderson–Kim resistivity theory (for details, see Supplementary Note 2). In addition, the obtained values of H_{c2}, U, and H_0 in the H // *ab* plane are 160–200% larger than those in H // *c*-axis, showing the anisotropic nature of flux pinning in $AuSn_4$, which is commonly observed in layered-structure superconductors, and is much smaller than those of superconducting iron pnictides and cuprates[39,40]. Therefore, the different properties of $AuSn_4$ between out-of-plane and in-plane magnetic fields should originate from the anisotropic nature, and means that the intrinsic pinning between the Au–Sn layers is dominant for the H // *ab* plane, and is stronger than extrinsic pinning due to stacking faults or defects for the H // *c*-axis.

BKT transition. It is well known that the 2D nature of the observed superconductivity can be confirmed by testing whether the electrical transport properties possess a signature of a BKT transition that can be characterized by a BKT temperature T_{BKT}, below which a phase transition leading to a 2D topological order emerges[3,41,42]. Figure 5a displays the I–V isotherms of a $AuSn_4$ single crystal on a log–log scale. The straight lines in this plot indicate the power-law behaviors, with the powers α equal to the slopes of the lines (i.e., $V \propto I^{\alpha}$). As seen, the I–V curves with a

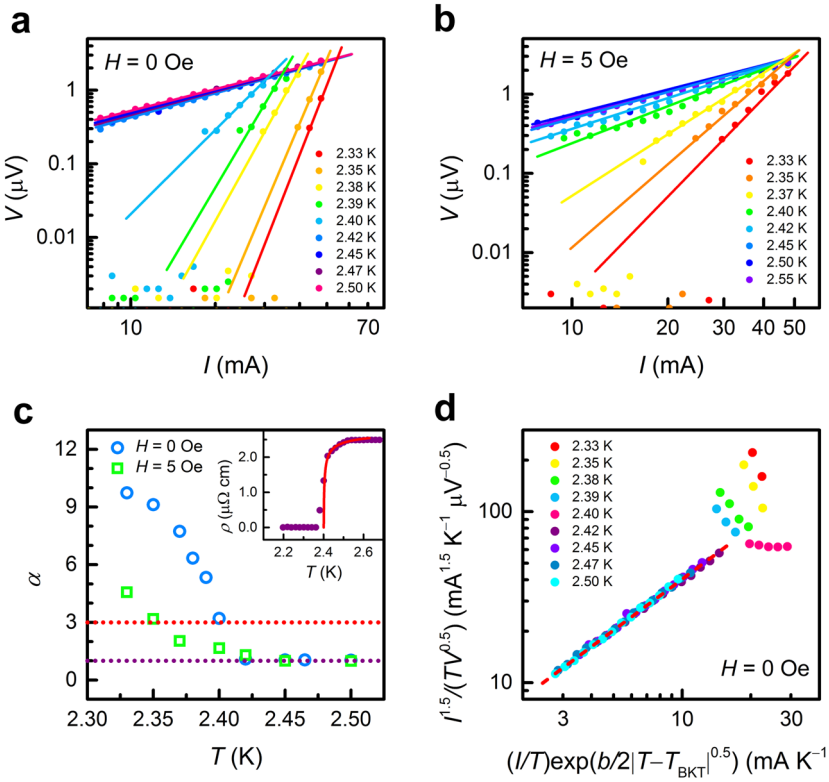

Fig. 5 BKT nature of $AuSn_4$. *I*–*V* isotherms of an $AuSn_4$ single crystal on a ln–ln scale with: **a** a zero field and **b** an applied field of 5 Oe. The straight lines are power-law fits to the data at different temperatures. **c** Temperature dependence of the power-law exponent α deduced from the power-law fits in **a** and **b**. Dashed lines denote the α values of 3 (red) and 1 (purple), respectively. The inset shows the ρ–T curve near the T_{BKT} regime that can be well fitted with HN relation, as illustrated by the solid line. **d** Scaled plot of $\frac{I}{T}\left(\frac{I}{V}\right)^{1/2}$ as a function of the scaling function variable $\frac{I\xi}{T}$ for data in **a**. The dashed line represents the best collapse onto a scaling curve at temperatures above T_{BKT}.

slope of 1 coincides with the high-temperature isotherms at temperatures above 2.40 K, which indicates their ohmic characteristics, while the *I*–*V* curve with a slope of 3 marks the initiation of a BKT transition, $V \propto I^3$; the slopes of the lines then increase drastically at lower temperatures. Notice that, due to the studied bulk single-crystal samples, there is no obviously finite-size-induced linear tail in the *I*–*V* data, as is usually observed in thin-film samples, such as one-unit-cell FeSe films[43] or $YBa_2Cu_3O_{7-\delta}$ films[44]. Thus, fitting is usually applied to the upper portion of the dataset, meaning just below the critical currents, as conducted for the Bi_2Te_3/FeTe heterostructure[20] and Mo_2C crystals[8]. As is known, the standard BKT transition is carried out in zero magnetic field, characterized by the thermally driven vortex–anti-vortex pairs unbinding at temperatures above T_{BKT}[41,42], while the vortex–anti-vortex pairs will break down in the presence of magnetic fields. Figure 5b shows the corresponding *I*–*V* isotherms with an applied field of 5 Oe; one can see that the slopes of the lines increase gradually as temperature decreases. Figure 5c shows the temperature dependence of the power-law exponent α deduced from the power-law fits in Fig. 5a, b. In Fig. 5c, the zero-field value of α approaches 3 at the temperature of 2.40 K, which is thus close to T_{BKT}; it increases rapidly for temperatures lower than 2.40 K, while the 5-Oe value of α increases continuously from 1.0 to 4.6 as the temperature decreases from 2.45 to 2.33 K. These observations are regarded as the hallmark of a BKT transition, which is surprisingly observed on a "bulk" $AuSn_4$ single crystal. In the infinite-size homogeneous case, a jump is expected from $\alpha = 3$ to $\alpha = 1$, as shown in Fig. 5c, whereas for both the one-unit-cell FeSe films[43] and Bi_2Te_3/FeTe heterostructure sample[20], the α value seems to show a smooth transition rather than a sudden sharp jump. Recalling the sharp resistive transition, as shown in Fig. 2f, it is expected that the BKT transition, which occurs at the temperature of 2.40 K, should be close to the resistive transition temperature of 2.42 K, as presented. Moreover, as described by the BKT theory for a 2D superconductor, the temperature-dependent resistivity at zero field is predicted to be in a form of the Halperin–Nelson (HN) relation[45] at temperatures just above T_{BKT}: $\rho(T) = \rho_n \exp(-bt^{-1/2})$, where ρ_n and b are material-specific parameters, and $t = T - T_{BKT}$ is the temperature deviation. As shown in the inset of Fig. 5c, the ρ–T curve near the T_{BKT} regime can be well fitted with HN relation and $b = 0.048\ K^{1/2}$, giving evidence of the 2D nature of superconductivity. Furthermore, a scaling ansatz has been proposed by Fisher et al.[46] for a general analysis of a superconducting phase transition in D dimensions using a dynamic scaling argument. This successful ansatz has been applied to a wide variety of systems and transitions, including 2D superconductors, Josephson-junction arrays, and superfluids[47], using the experimentally determined quantities V and I, $\frac{I}{T}\left(\frac{I}{V}\right)^{\left(\frac{1}{z}\right)} = F_{\pm}\left(\frac{I\xi}{T}\right)$, where ξ is the coherence length, $F_{\pm}$ are scaling functions above and below the transition, and $z = 2$ in a dynamic scaling analysis of 2D system *I*–*V* data. At this point, all that is required to do dynamic scaling is the temperature dependence of ξ, which can be defined above the transition as the size of a fluctuation or as the average distance between two free vortices and has been given by $\xi \propto \exp\left(\frac{b}{2\sqrt{|T-T_{BKT}|}}\right)$ with the constant b previously presented in the HN relation[46,47]. This scaling approach has been used to as a measure of proof of the existence or absence of a BKT transition; in effect, if the properly scaled current–voltage (*IV*) curves collapse (do not collapse) onto universal scaling curves above and below the transition, then a BKT transition is likely (unlikely) to be

present. In Fig. 5d we plot $\frac{I}{T}\left(\frac{I}{V}\right)^{1/2}$ as a function of the scaling function variable $\frac{I\xi}{T}$ for data in Fig. 5a and vary the fitting parameter T_{BKT} to achieve the best collapse onto a scaling curve. With $T_{BKT} =$ 2.401 K, which is a little lower than T_c of 2.421 K determined by the resistive transition, the scaling data present an acceptable scaling collapse (do not collapse) above (below) the transition T_{BKT}, agreeing well with the expected BKT behavior near the transition. One may notice that the scaling data at $T = 2.40$ K shows a nearly constant value, which can be understood by taking account of $V \propto I^3$ at $T =$ 2.40 K $\approx T_{BKT,}$ leading to an invariant term of $\frac{I}{T}\left(\frac{I}{V}\right)^{1/2}$ ($\propto I^{1.5}/V^{0.5}$) at a fixed temperature. These two resulting T_{BKT} values respectively derived from the HN relation and universal scaling are highly consistent with the value extracted from the power analysis that $\alpha \approx 3$ at $T = 2.40$ K. Our analysis thus provides strong evidences for a 2D nature of the observed superconductivity in $AuSn_4$.

Normal-state WAL transport properties. The 2D nature of the observed superconductivity in $AuSn_4$ will lead us further into considering the origin of 2D superconductivity. Since $AuSn_4$ is isostructural with the Dirac nodal arc semimetals $PtSn_4$ and $PdSn_4$, the origin of natural 2D superconductivity in $AuSn_4$ can be inferred from Dirac-like surface band dispersion. Thus, the normal-state transport properties of $AuSn_4$ are worth studying. Figure 6a shows a result of resistivity with applied fields parallel to the crystal *c*-axis. As shown, the $\rho(H)$ increases with the applied fields, and a clear non-saturating field-dependent magnetoresistance MR(H), defined as $MR(H) = [\rho(H) - \rho(0)]/\ \rho(0)$, can be seen for temperatures up to 50 K and field up to 6 T, as shown in Fig. 6b. A sharp normal-state resistivity dip is clearly observed at lower temperatures, even at temperatures above T_c or $H > H_{c2}$; when the temperature increases, the resistivity dip at low fields is broadened and the MR(H) becomes linear at an intermediate field in the whole normal-state region. It is known that a sharp magnetoresistance dip at low temperatures indicates the presence of a WAL effect; when we increase the temperature, the magnetoresistance dip broadens at the low field due to the decrease of the phase coherence length at higher temperatures[48]. Similar types of magnetoresistance behavior without any sign of saturation have been seen in topological materials[48–50]. In particular, Shrestha et al.[49] have recently shown extremely large non-saturating magnetoresistance (540% at $T = 2$ K under 7 T) and ultrahigh Hall mobility (4.5×10^4 cm^2 V^{-1} s^{-1} at $T = 5$ K) due to topological surface states in the metallic Bi_2Te_3 topological insulator[49], results which are comparable with those of magnetoresistance ≈ 650% at 2.5 K under 6 T and Hall mobility ≈ 3.5×10^3 cm^2 V^{-1} s^{-1} at $T = 2.5$ K observed on our $AuSn_4$ single crystals (for details, see Supplementary Note 3). We may also note that, due to the non-negligible contribution of transverse resistivity, as arising from the high Hall mobility, the original experimental resistivity data were asymmetric in the field. According to the argument proposed by Segal et al.[51], the odd longitudinal resistivity can be eliminated via counting the average experimental data in the positive and negative fields, leading to a duplicate result of magnetoresistance in the positive and negative fields, as shown in Fig. 6a, b, respectively. Additionally, in the $\rho(H)$ curves at $T < 3.75$ K, a crossover of $\rho(H)$ values from a downward-trend field dependence to a nearly linear H dependence can be observed when the magnetic field is beyond a crossover field H^*. The crossover field H^* can be determined by the plot of an intersection of two linear fitting lines, as shown by the two guide lines in Fig. 6a. One can see that the H^* shifts to a lower field with the increase in temperature, as shown in the inset of Fig. 6a. The temperature dependence of the H^* suggests the existence of a linear-dispersion electronic band in $AuSn_4$, as seen

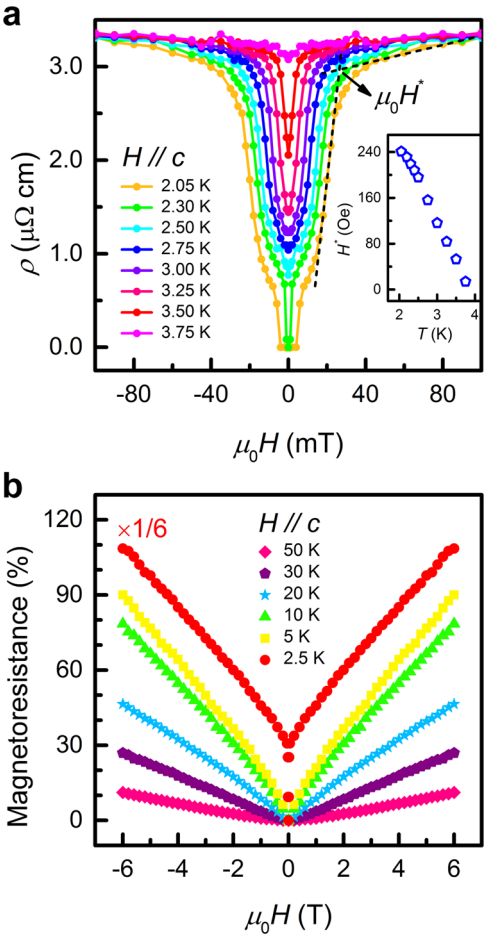

Fig. 6 Magnetoresistance of $AuSn_4$. a Resistivity with applied fields parallel to the crystal *c*-axis at various temperatures. The intersection of two dashed lines denotes the determination of the crossover field H^*. The inset shows the temperature dependence of H^*, as obtained from data in **a**. **b** Non-saturating MR(H) for temperature up to 50 K and field of up to 6 T. Note the drastic increase in magnetoresistance at 2.5 K plotted with a contracted scale of MR(H) × 1/6. Also note that the data show a duplicate result of magnetoresistance in positive and negative fields, as described in the text.

in topological materials[48–50]. Now that the normal-state transport property of $AuSn_4$ indicates a crossover from a WAL-dominant MR(H) to a linear and non-saturating MR(H), the field-dependent transverse magnetoconductivity will be analyzed within the framework of a WAL electrical transport. Figure 7 shows the field-dependent transverse magnetoconductivity change ratio for $AuSn_4$ at low temperatures, where the magnetoconductivity change ratio ΔMC is defined as $\Delta MC = [\sigma(H) - \sigma(0)]/\sigma(0)$. As is known, the transverse magnetoconductivity can be expressed by $\sigma_T(H) = \sigma_{WAL} + \sigma_n$, where σ_{WAL} is the surface conductivity from WAL corrections related with intranodal scattering, and σ_n is from conventional Fermi surface contributions[52]. The WAL formula is expressed as $\sigma_{WAL} = a\sqrt{H} + \sigma_0$ and $\sigma_n = (\rho_n + A{\cdot}H^2)^{-1}$, where a, σ_0, ρ_n, and A are determined from the line of best fitting. As seen, the low-field transverse ΔMC can be well described by the WAL transport formula with a negligible value of $A \approx 0$. The inset of Fig. 7 shows the temperature dependence of the obtained a values. One can see that parameter a is negative due to a positive magnetoresistance and at higher temperatures; the decrease in $|a|$ values with an increase in

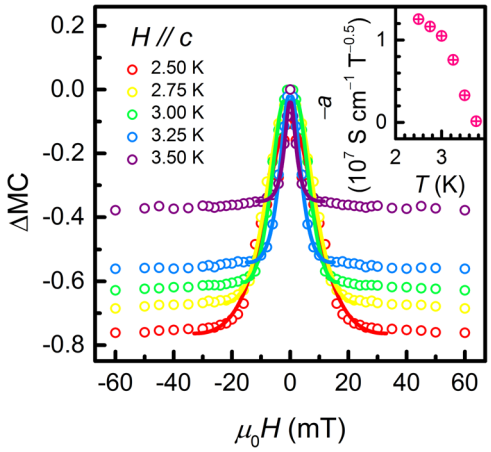

Fig. 7 Magnetoconductivity of $AuSn_4$. Field-dependent transverse magnetoconductivity change ratio for $AuSn_4$ at low temperatures. Solid lines denote the fitting of WAL formula. Inset: temperature dependence of obtained *a* values via the fitting of WAL formula.

temperature indicates a gradual absence of the WAL effect on the field-dependent transverse magnetoconductivity. It is known that in topological materials, strong spin–orbit coupling can induce WAL[53], and this WAL effect originates from the strong spin–orbit coupling in the band structure, and results in the spin-momentum locking in the topological surface states[54]. Therefore, the WAL phenomenon is always observed in topological materials as an important consequence of spin-momentum locking, as well as the full suppression of backscattering, which is a fingerprint of the surface states[55]. Since the normal-state transport properties of $AuSn_4$ exhibit the WAL behavior, one can deduce that $AuSn_4$ also belongs to the topological semimetals, same as its isostructural compounds of $PtSn_4$ and $PdSn_4$. All the results clearly prove that the natural 2D superconductivity in $AuSn_4$ originates from Dirac-like surface band dispersion, leading to the conclusion that topological superconductivity possibly exists on its surface and exhibits 2D nature. This work also provides important experimental results for further studies on the topological-semimetal candidate of $AuSn_4$, such as the theoretical band-structure calculation and angle-resolved photoemission spectroscopy experiments, which are popular topics in condensed matter physics.

Discussion

These presented results enabled us to construct a phase diagram of $AuSn_4$ crystals in the magnetic field-temperature (H–T) plane. The 2D superconductivity let us consider the emergence of the Bose-metal phase recently identified in 1T-MoS_2 and $NbSe_2$ (refs. [5,56]). Returning to the Arrhenius plot of resistivity, as shown in Fig. 8a, this study replotted some selected low-field Arrhenius plots of resistivity with H // c-axis, for a detailed discussion of the Bose-metal phase in $AuSn_4$. It has been pointed that a strongly disordered 2D superconductor makes a transition to an insulating state under a perpendicular magnetic field applied[57], while a system with a low disorder, such as a high-quality single crystal, should show a quantum phase transition to an intermediate 2D metallic state, Bose metal (BM), with a resistance much lower than the normal-state resistivity[6,57,58]. This state is characterized by saturation of the resistance as T approaches 0 K. Additionally, the resistance obeys a power law with the magnetic field, which has been theoretically addressed using a simple scaling of power-law BM resistivity[57], $\rho \propto (H - H_{c0})^{2\nu}$, where H_{c0} and ν are the critical field of $\sim H_{c1}(0)$ and the exponent of this step of the superconducting-BM transition, respectively. Figure 8a displays the possible existence of the BM phase in $AuSn_4$, where following on a sharp drop in resistivity at the superconducting transition point, the resistivity deviates from thermally activated behavior and gradually decreases to a small value compared to ρ_N as the temperature is lowered. The field resistivity does not exhibit a saturated constant value as seen in 1T-MoS_2 (ref. [5]), which should be due to the presence of bulk superconductivity. Thus, the deviation temperature T^* for finite field values as indicated in Fig. 8a can be deduced to define the BM phase in the 2D superconductivity regime. Also shown in Fig. 8b is a log–log scale plot of resistivity versus perpendicular magnetic field for temperatures below T_{BKT} with a fit to the power-law dependence by the use of $H_{c0} = 39.4$ Oe and $\nu = 2.18$–2.42 for different temperatures. This power-law resistivity demonstrates the possible existence of the BM phase in $AuSn_4$. For further confirming the BM phase of 2D superconductors, we adopted the Ullah–Dorsey (UD) scaling theory[59] to calculate the excess conductance generated by the fluctuation of the superconducting order parameter. The excess conductivity, $G_{fl} \equiv 1/\rho\ (T) - 1/\rho_N(T)$, under different magnetic field is scaled with the universal relation[60]:

$$G_{fl} \cdot \left(\frac{\mu_0 H}{T}\right)^{0.5} = F_{fl}\left(\frac{T - T_c(H)}{(\mu_0 H T)^{0.5}}\right),\ F_{fl}(x) \propto \begin{cases} -x (x \ll 0) \\ x^{-s} (x \gg 0) \end{cases}. \quad (3)$$

Here, $s = 1$ in the case of a 2D system, $T_c(H)$ is the mean field transition temperature in a magnetic field and $\rho_N(T)$ is the normal-state resistivity. As shown in Fig. 8c, by using $\rho(T)$ data in the presence of a magnetic field and taking $T_c(H)$ derived from the data corresponding to the temperature on the $H_{c2}(T)$ curve as previously obtained in Fig. 3a, it is found that $G_{fl}\cdot(\mu_0 H/T)^{0.5}$ curves with a fitting parameter ρ_N of ~2.564 μΩ cm for scaling in the $AuSn_4$ at $T > T_c(H)$ collapse onto a single curve with the slope of −1 in log–log plots, indeed obeying the 2D UD scaling law of Eq. (3). However, it must be noted that this kind of metallic state can also be interpreted as a result of quantum creep, as seen in a ZrNCl electric-double-layer transistor[7]. In this model, the sheet resistance R_s in the limit of the strong dissipation obeys a general form[61]:

$$R_s \frac{\hbar}{4e^2}\frac{\kappa}{1-\kappa} \text{ with } = \exp\left[C\frac{\hbar}{e^2}\frac{1}{R_N}\left(\frac{H - H_{c2,c}}{H_{c2,c}}\right)\right], \quad (4)$$

where R_N is the normal-state sheet resistance and C is a dimensionless constant. According to Eq. (4), it can be predicted that the term $\ln\left(1 + \frac{1}{R_s}\frac{\hbar}{4e^2}\right)$ should be in proportion to $\frac{H_{c2,c}-H}{H_{c2,c}}$, and will show a linear relationship passing through the origin point. However, as seen in Fig. 8d, the plots of the $\ln(1 + \frac{1}{R_s}\frac{\hbar}{4e^2}) - \frac{H_{c2,c}-H}{H_{c2,c}}$ relation at temperatures of 2.05 and 2.20 K cannot be well fitted to Eq. (4) for a wide range by adjusting the C value; thus, an extra constant C_0 is required for linear fitting, i.e., the relationship does not pass through the origin point. This result indicates that the quantum-creep model does not apply to the $AuSn_4$ case. Summarizing these results of $H_{c1,c}(T)$, $T^*(H)$, $H_{c2,c}(T)$, and the normal-state $H^*(T)$, we can construct a phase diagram of $AuSn_4$ crystals in the H–T plane, as presented in Fig. 9, displaying different regimes of transport arising due to vortex dynamics and surface Dirac linear dispersion. The normal state is divided by $H^*(T)$, according to the crossover from a WAL-dominant transport (shaded in orange) to a linear and non-saturating magnetoresistance transport (shaded in red). The 2D superconducting phase is separated from the normal state by the $H_{c2,c}(T)$ line. As the temperature is lowered below T_c, $AuSn_4$ goes into a 2D thermally activated flux flow (TAFF) regime (shaded in yellow), where the resistivity exhibits an activated behavior due to temperature-

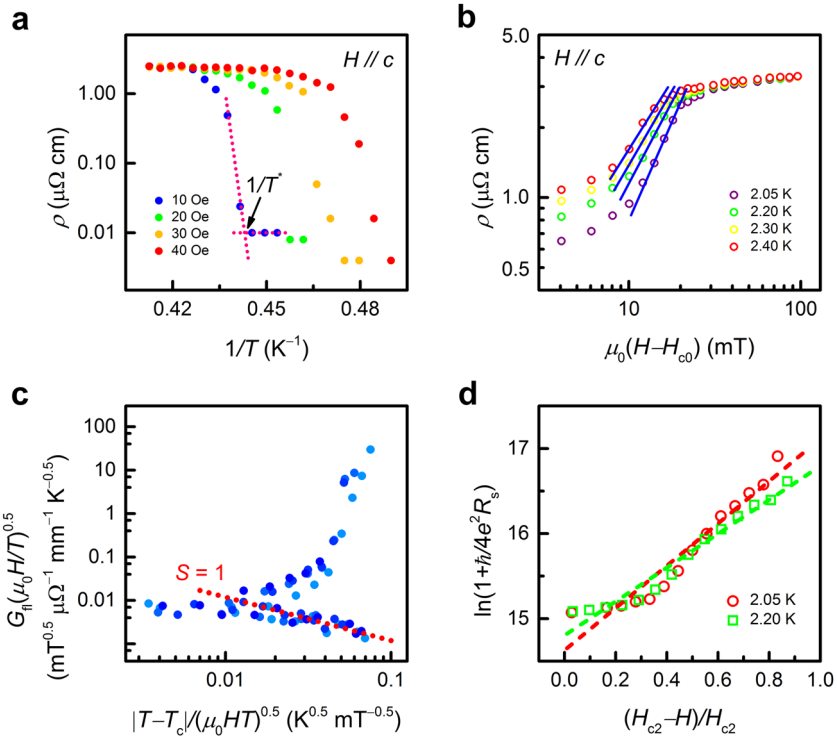

Fig. 8 Characteristics of Bose-metal phase in $AuSn_4$. **a** Details of some selected low-field Arrhenius plots of resistivity with H // c-axis, where dashed lines illustrate the resistivity deviation from the thermally activated behavior to a small value at temperature T^*, as compared to the normal-state resistivity. **b** A log–log scale plot of resistivity vs. perpendicular magnetic field $\mu_0(H-H_{c0})$ for temperatures below T_{BKT}. Solid lines represent the fit to the power-law dependence, as described in the text. **c** Ullah–Dorsey scaling of fluctuation conductivity using the $\rho(T)$ data in the presence of a magnetic field. The dashed line indicates the slope of −1 in a log–log plot. **d** Plots of the $\ln\left(1+\frac{1}{R_s}\frac{\hbar}{4e^2}\right)-\frac{H_{c2,c}-H}{H_{c2,c}}$ relation at temperatures of 2.05 and 2.20 K, where the dashed lines represent the linear fit to Eq. (4) with an extra constant C_0, where $C_0 = 14.63$ and 14.80 for 2.05 and 2.20 K, respectively.

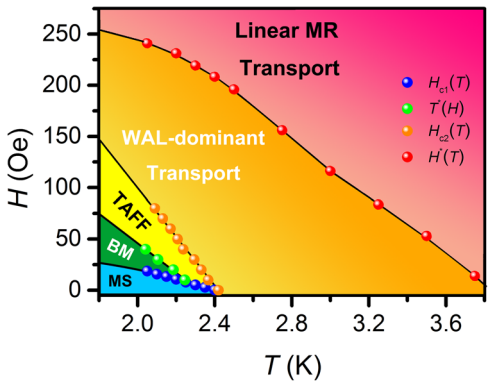

Fig. 9 Phase diagram of $AuSn_4$ crystals in the H–T plane. Phase diagram of $AuSn_4$ crystals in the H–T plane via summarizing the results of $H_{c1,c}(T)$, $T^*(H)$, $H_{c2,c}(T)$, and the normal-state $H^*(T)$. The normal state is divided by $H^*(T)$, showing the crossover from a WAL-dominant transport (shaded in orange) to a linear and non-saturating magnetoresistance transport (shaded in red). The 2D superconducting phase is separated from the normal state by $H_{c2,c}(T)$ line and consists of a 2D TAFF regime (shaded in yellow) and a BM regime (shaded in green) separated by the temperature $T^*(H)$. At sufficiently low temperatures and magnetic fields, the subsequent BCS bulk-superconductivity Meissner state (MS, shaded in blue) is characterized by the $H_{c1,c}(T)$ line.

driven depairing of the vortex–anti-vortex pairs. The boundary between the TAFF and the BM (shaded in green) regimes is defined by the temperature $T^*(H)$, which characterizes the finite resistive dissipation at higher magnetic fields. At sufficiently low temperatures and magnetic fields, the subsequent BCS bulk-superconductivity Meissner state (MS, shaded in blue) is characterized by the $H_{c1,c}(T)$ line. Compared to conventional BCS type-II superconductors, our results show that the presence of Dirac-like surface band dispersion in $AuSn_4$ crystals gives rise to a nontrivial 2D superconducting phase in the phase diagram, exerting a drastic impact on the possible topological superconductivity in $AuSn_4$.

In summary, the dimensionality of superconductivity in $AuSn_4$ single crystals has been explored herein. The bulk superconductivity with the T_c of ~2.40 K probed by the magnetization and special heat measurements reveals a characteristic of conventional BCS type-II superconductors. However, the superconductivity investigated with electrical transport properties exhibits 2D nature by showing evidence of a BKT transition, BM phase, and the diverging ratio of in-plane to out-plane upper critical field on approaching T_c. The vortex dynamics of $AuSn_4$ further display that the activation energy $U(H)$ and upper critical field $H_{c2}(T)$ can be interpreted in terms of the TAFF model in two dimensions. Moreover, it is found that in the normal state, the low-temperature magnetoconductivity of $AuSn_4$ can be well described by the WAL transport formula, which has been commonly observed on topological materials; thus, it strongly supports the scenario that the surface electrons in Dirac-cone states dominate the normal-state magnetotransport in $AuSn_4$ single crystals. The results clearly prove that the natural 2D superconductivity in $AuSn_4$ originates from Dirac-like surface band dispersion, leading to the conclusion that topological superconductivity possibly exists on its surface and exhibits 2D nature. Finally, a phase diagram of $AuSn_4$ crystals in the H–T plane has been constructed, which displays different regimes of transport arising due to the vortex dynamics and surface Dirac linear

dispersion, drastically impacting the possible topological superconductivity in $AuSn_4$.

Methods

Single-crystal growth. $AuSn_4$ single crystals were grown from Sn flux with a starting composition of Au:Sn = 0.09:0.91. The mixtures of high-purity Au pieces and Sn ingots were sealed under vacuum in a quartz tube. The quartz ampoule was heated to 630 °C for 10 h, cooled to 310 °C for 6 h and then slowly cooled down to 240 °C at a rate of 1 °C per hour. The remaining Sn flux was separated by centrifugation and several platelet-like crystals with a typical size of $3 \times 2 \times 0.3$ mm^3 were mechanically removed from the quartz ampoule. The as-grown crystals are ductile and exhibit a silvery luster. However, they cannot be mechanically exfoliated to be a few-layer thickness like graphene. The $AuSn_4$ crystals are stable in air over months but corrode in diluted hydrochloric acid. The phase purity and the crystal structure of obtained crystals were characterized by powder X-ray diffraction (Bruker D2 phaser) and Laue diffraction (Photonic Science) measurements with Cu-K_α radiation on single crystals.

Transport measurements. For in-plane electrical transport measurements, the cleaved shiny crystals were cut into dimensions of ~$3.0 \times 1.0 \times 0.1$ mm^3. Five leads were soldered with indium, and a Hall-measurement geometry was formed to allow simultaneous measurements of both longitudinal (ρ) and transverse (Hall) resistivities (ρ_{xy}) using the standard dc four-probe technique. Hall voltages were taken in opposing fields parallel to the c-axis up to 6 T and at a dc current density of ~30 A cm^{-2}. The low-temperature specific heat C_p measurement was carried out using a ^{3}He heat-pulsed thermal relaxation calorimeter (PPMS-16 from Quantum Design) in the temperature range of 0.5–3.0 K. The magnetization was measured in a superconducting quantum interference device (SQUID) system (MPMS from Quantum Design).

Data availability

The data that support the findings of this study are available on reasonable request.

Received: 6 February 2020; Accepted: 1 July 2020;
Published online: 12 August 2020

References

1. Weitering, H. H. & Wu, J. Z. Superconductivity: how the unconventional became the new norm preface. *Supercond. Sci. Technol.* **30**, 040301 (2017).
2. Saito, Y., Nojima, T. & Iwasa, Y. Highly crystalline 2D superconductors. *Nat. Rev. Mater* **2**, 16094 (2016).
3. Reyren, N. et al. Superconducting interfaces between insulating oxides. *Science* **317**, 1196 (2007).
4. Fogel, N. Y. et al. Direct evidence for interfacial superconductivity in two-layer semiconducting heterostructures. *Phys. Rev. B* **73**, 161306 (2006).
5. Sharma, C. H., Surendran, A. P., Varma, S. S. & Thalakulam, M. 2D superconductivity and vortex dynamics in 1T-MoS_2. *Commun. Phys.* **1**, 90 (2018).
6. Tsen, A. W. et al. Nature of the quantum metal in a two-dimensional crystalline superconductor. *Nat. Phys.* **12**, 208 (2016).
7. Saito, Y. et al. Metallic ground state in an ion-gated two-dimensional superconductor. *Science* **350**, 409 (2015).
8. Liu, Z. et al. Effects of domain structures on vortex state of two-dimensional superconducting Mo_2C crystals. *2D Mater* **6**, 021005 (2019).
9. Cui, J. et al. Transport evidence of asymmetric spin–orbit coupling in few-layer superconducting 1Td-$MoTe_2$. *Nat. Commun.* **10**, 2044 (2019).
10. Tian, W., Yu, W., Shi, J. & Wang, Y. The property, preparation and application of topological insulators: a review. *Materials* **10**, 814 (2017).
11. Chang, G. et al. Nexus fermions in topological symmorphic crystalline metals. *Sci. Rep.* **7**, 1688 (2017).
12. Sato, M. & Ando, Y. Topological superconductors: a review. *Rep. Prog. Phys.* **80**, 076501 (2017).
13. Qi, X. L. & Zhang, S. C. Topological insulators and superconductors. *Rev. Mod. Phys.* **83**, 1057–1110 (2011).
14. Alicea, J. New directions in the pursuit of Majorana fermions in solid state systems. *Rep. Prog. Phys.* **75**, 076501 (2012).
15. Nayak, C. et al. Non-Abelian anyons and topological quantum computation. *Rev. Mod. Phys.* **80**, 1083–1159 (2008).
16. Fu, L. & Kane, C. L. Superconducting proximity effect and Majorana fermions at the surface of a topological insulator. *Phys. Rev. Lett.* **100**, 096407 (2008).
17. Sasaki, S. et al. Topological superconductivity in $CuxBi_2Se_3$. *Phys. Rev. Lett.* **107**, 217001 (2011).
18. Wang, M. X. et al. The coexistence of superconductivity and topological order in the Bi_2Se_3 thin films. *Science* **336**, 52 (2012).
19. Qu, F. et al. Strong superconducting proximity effect in Pb-Bi_2Te_3 hybrid structures. *Sci. Rep.* **2**, 339 (2012).
20. He, Q. L. et al. Two-dimensional superconductivity at the interface of a Bi_2Te_3/FeTe heterostructure. *Nat. Commun.* **5**, 4247 (2014).
21. Liu, H. C. et al. Robust two-dimensional superconductivity and vortex system in Bi_2Te_3/FeTe heterostructures. *Sci. Rep.* **6**, 26168 (2016).
22. Zhang, P. et al. Observation of topological superconductivity on the surface of an iron-based superconductor. *Science* **360**, 182 (2018).
23. Mun, E. et al. Magnetic field effects on transport properties of $PtSn_4$. *Phys. Rev. B* **85**, 035135 (2012).
24. Wu, Y. et al. Dirac node arcs in $PtSn_4$. *Nat. Phys.* **12**, 667 (2016).
25. Xu, C. Q. et al. Enhanced electron correlations in the binary stannide $PdSn_4$: a homologue of the Dirac nodal arc semimetal PtSn4. *Phys. Rev. Mater.* **1**, 064201 (2017).
26. Jo, N. H. et al. Extremely large magnetoresistance and Kohler's rule in PdSn4: a complete study of thermodynamic, transport, and band-structure properties. *Phys. Rev. B* **96**, 165145 (2017).
27. Kubiak, R., Woz.xl & Lcyrz, M. Refinement of the crystal structures of $AuSn_4$ and $PdSn_4$. *J. Less Common Met.* **97**, 265–269 (1984).
28. Kubiak, R. & Wołcyrz, M. X-ray investigations of crystallization and thermal expansion of $AuSn_4$, $PdSn_4$ and $PtSn_4$. *J. Less Common Met.* **109**, 339–344 (1985).
29. Gendron, M. F. & Jones, R. E. Superconductivity in the $CuAl_2$ (C16) crystal class. *J. Phys. Chem. Solids* **23**, 405–406 (1962).
30. Raub, C. Superconductivity of the noble metals and their alloys. *Z. Metallk.* **55**, 195 (1964).
31. Jin, B. B. et al. Energy gap, penetration depth, and surface resistance of MgB_2 thin films determined by microwave resonator measurements. *Phys. Rev. B* **66**, 104521 (2002).
32. Kim, M. et al. Intrinsic spin-orbit coupling in superconducting δ-doped $SrTiO_3$ heterostructures. *Phys. Rev. B* **86**, 085121 (2012).
33. Yan, R. et al. GaN/NbN epitaxial semiconductor/superconductor heterostructures. *Nature* **555**, 183 (2018).
34. Tinkham, M. *Introduction to Superconductivity*. 2nd edn (Dover, New York, 2004).
35. Blatter, G., Geshkenbein, V. B. & Larkin, A. I. From isotropic to anisotropic superconductors: a scaling approach. *Phys. Rev. Lett.* **68**, 875 (1992).
36. Anderson, P. W. & Kim, Y. B. Hard superconductivity: theory of the motion of Abrikosov flux lines. *Rev. Mod. Phys.* **36**, 39–43 (1964).
37. Lei, H. et al. Thermally activated energy and flux-flow Hall effect of $Fe_{1+y}(Te_{1+x}S_x)_z$. *Phys. Rev. B* **82**, 134525 (2010).
38. Feigel'man, M. V., Geshkenbein, V. B., Larkin, A. I. & Vinokur, V. M. Theory of collective flux creep. *Phys. Rev. Lett.* **63**, 2303–2306 (1989).
39. Ahmad, D. et al. Thermally activated flux flow in superconducting epitaxial $FeSe_{0.6}Te_{0.4}$ thin film. *Results Phys.* **7**, 16–20 (2017).
40. Yang, H. C., Wang, L. M. & Horng, H. E. Characteristics of flux pinning in YBa_2Cu_3Oy /$PrBa_2Cu_3Oy$ superlattices. *Phys. Rev. B* **59**, 8956–8961 (1999).
41. Kosterlitz, J. M. & Thouless, D. J. Ordering, metastability and phase transitions in two-dimensional systems. *J. Phys. C Solid State Phys.* **6**, 1181–1203 (1973).
42. Kosterlitz, J. M. The critical properties of the two-dimensional xy model. *J. Phys. C Solid State Phys.* **7**, 1046–1060 (1974).
43. Zhang, W. H. et al. Direct observation of high-temperature superconductivity in one-unit-cell FeSe films. *Chin. Phys. Lett.* **31**, 017401 (2014).
44. Repaci, J. M. et al. Is there a Kosterlitz-Thouless transition in YBCO films? *Physica C* **282–287**, 2081–2082 (1997).
45. Halperin, B. I. & Nelson, D. R. Resistive transition in superconducting films. *J. Low Temp. Phys.* **36**, 599–616 (1979).
46. Fisher, D. S., Fisher, M. P. A. & Huse, D. A. Thermal fluctuations, quenched disorder, phase transitions, and transport in type-II superconductors. *Phys. Rev. B* **43**, 130–159 (1991).
47. Pierson, S. W. et al. Dynamic scaling for two-dimensional superconductors, Josephson-junction arrays, and superfluids. *Phys. Rev. B* **60**, 1309–1325 (1999).
48. He, H. T. et al. Impurity effect on weak antilocalization in the topological insulator Bi_2Te_3. *Phys. Rev. Lett.* **106**, 166805 (2011).
49. Shrestha, K. et al. Extremely large nonsaturating magnetoresistance and ultrahigh mobility due to topological surface states in the metallic Bi2Te3 topological insulator. *Phys. Rev. B* **95**, 195113 (2017).
50. Singh, A. et al. Enhancement in power factor due to anti-correlation between electrical conductivity and thermoelectric power and induced magnetic ordering in high mobility Zn doped Bi_2Te_3 topological insulator. *J. Alloys Compd.* **731**, 297–302 (2018).
51. Segal, A. et al. Asymmetric field dependence of magnetoresistance in magnetic films. *Phys. Rev. B* **79**, 144434 (2009).
52. Kim, H. J. et al. Dirac versus Weyl fermions in topological insulators: Adler-Bell-Jackiw anomaly in transport phenomena. *Phys. Rev. Lett.* **111**, 246603 (2013).

53. Liu, W. E., Hankiewicz, E. M. & Culcer, D. Weak localization and antilocalization in topological materials with impurity spin-orbit interactions. *Materials* **10**, 807 (2017).
54. Nomura, K., Koshino, M. & Ryu, S. Topological delocalization of two-dimensional massless dirac Fermions. *Phys. Rev. Lett.* **99**, 146806 (2007).
55. Fanga, L. & Kwok, W. K. Quantum phenomena in transport measurements of topological insulator nanostructures. *Low Temp. Phys.* **40**, 280 (2014).
56. Ichinokura, S. et al. Vortex-induced quantum metallicity in the mono-unit-layer superconductor $NbSe_2$. *Phys. Rev. B* **99**, 220501 (2019).
57. Das, D. & Doniach, S. Bose metal: gauge-field fluctuations and scaling for field-tuned quantum phase transitions. *Phys. Rev. B* **64**, 134511 (2001).
58. Saito, Y., Nojima, T. & Iwasa, Y. Quantum phase transitions in highly crystalline two-dimensional superconductors. *Nat. Commun.* **9**, 778 (2018).
59. Ullah, S. & Dorsey, A. T. Critical fluctuations in high-temperature superconductors and the Ettingshausen effect. *Phys. Rev. Lett.* **65**, 2066–2069 (1990).
60. Theunissen, M. H. & Kes, P. H. Resistive transitions of thin film superconductors in a magnetic field. *Phys. Rev. B* **55**, 15183–15190 (1997).
61. Shimshoni, E., Auerbach, A. & Kapitulnik, A. Transport through quantum melts. *Phys. Rev. Lett.* **80**, 3352–3355 (1998).

Acknowledgements

The authors thank the National Science Council of the Republic of China for financial support under grant numbers MOST 107-2112-M-002-018 and MOST 106-2112-M-006-013-MY3.

Author contributions

C.N.K. synthesized the single crystals and performed XRD and special heat measurements. T.W.Y. and I.N.C. performed magnetic susceptibility. D.S. and L.M.W. performed electrical transport measurements. C.N.K., D.S., and L.M.W. analyzed the data. L.M.W. wrote the manuscript. C.S.L. and L.M.W. supervised the project.

Competing interests

The authors declare no competing interests.

Additional information

Supplementary information is available for this paper at https://doi.org/10.1038/s43246-020-00060-8.

Correspondence and requests for materials should be addressed to L.M.W.

Reprints and permission information is available at http://www.nature.com/reprints

Publisher's note Springer Nature remains neutral with regard to jurisdictional claims in published maps and institutional affiliations.